CORA Cork Open Research Archive
Cartlann Taighde Oscailte Chorcaí

Title	A portable multiplexed electrochemical biosensor for lactate and pH monitoring in calf saliva
Authors	Adib, Md Ridwan;Higes-Marquez, Javier;Barrett, Colm;O'Sullivan, Shane;McFadden, Marie;Kennedy, Emer;O'Riordan, Alan
Publication date	2026-11-01
Original Citation	Adib, M R, Higes-Marquez, J, Barrett, C, O'Sullivan, S, McFadden, M, Kennedy, E & O'Riordan, A 2026, 'A portable multiplexed electrochemical biosensor for lactate and pH monitoring in calf saliva', Biosensors and Bioelectronics, vol. 311, 118965, pp. 1-11. https://doi.org/10.1016/j.bios.2026.118965
Type of publication	Article (peer-reviewed)
Link to publisher's version	https://www.scopus.com/pages/publications/105042793663 - 10.1016/j.bios.2026.118965
Rights	© 2026, authors. Published by Elsevier B.V. This is an open access article under the CC BY license (http://creativecommons.org/licenses/by/4.0/) - https://creativecommons.org/licenses/by/4.0/
Download date	2026-11-14 00:06:54
Item downloaded from	https://hdl.handle.net/10468/19616



UCC
University College Cork, Ireland
Coláiste na hOllscoile Corcaigh

Supplementary data

A Portable Multiplexed Electrochemical Biosensor for Lactate and pH Monitoring in Calf Saliva

Md Ridwan Adib[1*], Javier Higes-Marquez[1], Colm Barrett[1], Shane O'Sullivan[1], Marie McFadden[2], Emer Kennedy[2], Alan O'Riordan[1*]

[1]Precision Electrochemical Nanosensor Group, Tyndall National Institute, University College Cork, Dyke Parade, Cork, Ireland

[2]Teagasc, Animal & Grassland Research and Innovation Centre, Moorepark, Fermoy, Cork, Ireland

*Corresponding authors: alan.oriordan@tyndall.ie, ridwan.adib@tyndall.ie

1.1. Materials and reagents

Ferrocenecarboxylic acid (FCA), sodium phosphate monobasic (NaH_2PO_4), sodium phosphate dibasic (Na_2HPO_4), chloroplatinic acid hexahydrate ($H_2PtCl_6.6H_2O$), lead(II) acetate trihydrate ($Pb(CH_3COO)_2.3H_2O$), o-phenylenediamine (o-PD), sodium sulfate (Na_2SO_4), β-cyclodextrin (β-CD), hydrogen peroxide (H_2O_2, 30 wt %), L-(+)-Lactic acid, D-(+)-glucose, L-ascorbic acid (AA), uric acid (UA), D-(−)-fructose (D-Fruc), and acetaminophen (Ace) were purchased from Merck Life Science Ltd. Lactate oxidase (LOx, Aerococcus viridans, 20 U mg^{-1}) was obtained from Sekisui Diagnostics Ltd. (Maidstone, U.K.). Artificial saliva (medical and dental grade) was purchased from Pickering Laboratories (Mountain View, CA, U.S.A.). Calf saliva samples were collected at Teagasc, Animal & Grassland Research and Innovation Centre (Republic of Ireland). All chemical preparations and rinsing steps were performed using deionized Milli-Q water (18.2 MΩ·cm).

1.2. Instrumentation and experimental setup

Electrochemical measurements were carried out using a potentiostat (Autolab MULTI AUTOLAB M101, Metrohm Ltd., Utrecht, The Netherlands). All characterizations and electrode modifications were performed with the on-chip counter electrode (CE) and reference electrode (RE). A custom chip holder was fabricated using a Bridgeport Hardinge VMC 480 CNC machine to connect the silicon chip to the potentiostat. The chip incorporated gold IDE arrays (six individually addressable working electrodes, WEs), a gold macroband CE, and a platinum pseudo-RE. The IDEs were configured as sensor-protonator array, enabling a four-electrode setup for in situ electrochemical pH control experiments **(Fig. S1)**. A custom-designed sensor electronics interface was also employed for direct operation of the multiplexed chip and real-time electrochemical signal acquisition. Microscopic images were obtained using a Thorlabs camera coupled to a fluorescence trinocular microscope (DM RB Type 301-371.010, 501005/175257). Scanning electron microscopy (SEM) and energy-dispersive X-ray spectroscopy (EDX) were performed with a Zeiss Supra 40 system. Atomic force microscopy (AFM, Bruker) was conducted in ScanAsyst-air mode using a triangular silicon nitride cantilever with a reflective aluminum backside coating, and images were analyzed with Gwyddion software (v2.61). Lactate concentrations in artificial and real saliva samples were measured using a Lactate Pro 2 with test strips (Fitness Equipment Ireland). All collected data were processed and analyzed using OriginPro 2021.

1.3. Silicon chip fabrication process

The fabrication of the silicon-based interdigitated electrode (IDE) sensor chips was carried out on 4-inch silicon wafers. The wafers were first subjected to a standard cleaning procedure, involving sequential ultrasonication in acetone, isopropyl alcohol (IPA), and deionized (DI) water for 5 minutes each to remove organic residues and surface contaminants. Each wafer possessed a ~300 nm thermally grown silicon dioxide (SiO_2) insulating layer, deposited via plasma-enhanced chemical vapor deposition (PECVD) to serve as a passivation layer. A layer of S1813 photoresist (PR) was then spin-coated and patterned using Metal Mask-1 to define six individual IDE sensors. Following pattern development, a titanium/gold (Ti/Au) bilayer was deposited using electron beam evaporation (E-beam) with respective thicknesses of 20 nm and 150 nm. The subsequent lift-off process yielded well-defined comb-like Ti/Au IDE

microbands measuring 1 µm in width, 150 nm in height, and 80 µm in length. Next, Metal Mask-2 was employed for the photolithographic definition of contact pads, interconnection tracks (leads), and reference/counter electrode areas (approximately 500 µm wide and 10 mm long). A short ultrasonic lift-off (2-3 s) was applied to ensure clean feature definition. The process continued with Metal Mask-3, which included a dual-phase Ti/Au deposition to reinforce electrical contacts and define the sensing IDEs, leads, and both counter (CE) and reference (RE) electrodes. Subsequently, sequential deposition of titanium (Ti), nickel (Ni), and platinum (Pt) was carried out to fabricate the on-chip reference electrode, followed by lift-off. To insulate non-active regions, the wafer was coated with a 500 nm silicon nitride (Si_3N_4) layer. The reactive ion etching (RIE) technique was then employed to open windows selectively for the six sensing IDEs, CE/RE regions, and contact pads, using a passivation mask to protect other areas during etching. Finally, a protective photoresist layer (AR-PC 500) was applied to safeguard the wafer surface during the mechanical dicing step, which separated individual chips. The overall fabrication sequence is illustrated in **Fig. S1.** To ensure straightforward connectivity, each chip incorporated an on-chip microSD-style electrical interface, enabling rapid connection and replacement during electrochemical measurements. This plug-and-play design allowed for efficient chip interchange with the potentiostat, streamlining the analysis of multiple samples.

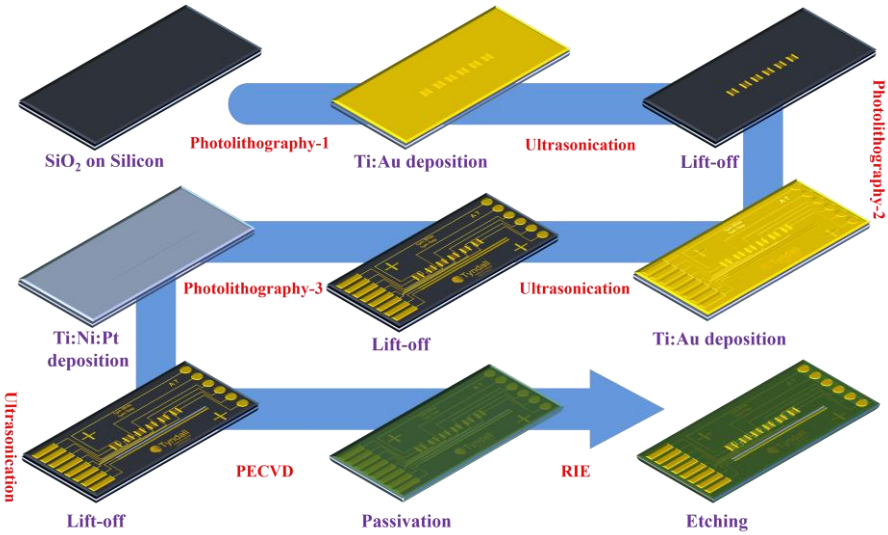


Fig. S1. Schematic illustration of the fabrication process of the proposed enzymatic lactate sensor.

1.4. Preparation of lactate sensor

Following the fabrication of the microband IDEs, individual chips (**Fig. 1a** in the main manuscript) were prepared for surface modification. Before modification, each sensor was thoroughly cleaned by sequential ultrasonication in acetone, isopropanol (IPA), and deionized (DI) water for 3–5 minutes each to remove any residual photoresist and surface contaminants. A representative optical image of a single working electrode is shown in **Fig. 1b**. The overall modification strategy (illustrated in **Fig. 1c**) was adapted from previously reported methods **(Barrett et al., 2019),** with minor adjustments for the present study. Considering the superior catalytic properties of platinum for water electrolysis, Pt was electrodeposited selectively on the protonator IDEs to promote efficient proton generation at reduced overpotentials. The platinum-black layer was deposited via CA from an aqueous solution containing 15 mM chloroplatinic acid hexahydrate and 2.4 mM lead (II) acetate trihydrate, applying a potential of -0.375 V versus the on-chip platinum pseudo-reference electrode for 120 s. Subsequently, an o-PD/β-CD)/LOx film was electropolymerized on the working electrodes by applying a potential of 0.7 V (vs. on-chip Pt RE) for 1200 s. The electro-polymerization was carried out in a mixed solution of 5 mM Na_2SO_4, 10 mM o-PD, 15 mM β-CD, and 10 mg/mL LOx prepared in 50 mM phosphate buffer (PB) (sodium phosphate monobasic and dibasic, pH 7.4) **(Fig. 1d)**. After modification, the electrodes were rinsed with 10 mM PB to remove loosely bound enzyme molecules. The modified chips were then stored in 50 mM PB (pH 7.4) at 4 °C overnight to allow stabilization of the enzyme layer and ensure consistent biosensor performance prior to testing.

1.5. Sensor characterization

Surface morphology and composition of the electrodes were examined using SEM, EDX, and AFM to compare the surface features of bare Au, Pt-black (Pt-B), Pt-B/o-PD/β-CD, and Pt-B/o-PD/β-CD/LOx modified electrodes. AFM imaging, was performed at a scan rate of 0.8 Hz over an area of 2.6 µm × 2.6 µm, acquired at 512 lines per second. This provided detailed surface topography and enabled determination of the root mean square (RMS) roughness, a parameter directly linked to surface structure and uniformity. To assess intra-chip reproducibility, CV measurements were performed in 1 mM FCA solution using six individual gold IDEs. The reproducibility was quantified by calculating the relative standard deviation (RSD%) according to: RSD% = (σ/µ) x 100, where σ represents the standard deviation and µ the mean of the limiting current values (n = 6). Further CV studies were conducted within the potential range of -0.2 V to 0.4 V at a scan rate of 50 mVs^{-1} using the generator-collector (GC) configuration. During these measurements, the protonator IDEs were held at 0 V, while the working IDEs were scanned across the potential range. To optimize sensor performance, the concentrations of o-PD (in mM) and lactate oxidase (LOx, in mg/mL) were systematically varied in response to the addition of 0.5 mM lactate. The pH-dependent enzyme activity of LOx was then evaluated across a broad range of pH 5.0 - 8.5 at 25 °C, using 2 mM lactate solution. Additional CV experiments were carried out in 0.8 mM H_2O_2 and 1 mM FCA to analyze electrochemical behavior at various modification stages. Electrochemical impedance spectroscopy (EIS) was employed after each surface modification step using 1 mM FCA in 10 mM PB. The charge transfer characteristics were examined across a frequency range of 0.3 Hz to 100 kHz, applying a potential of 0.2 V.

1.6. Generation of molecular oxygen

Faraday's first law of electrolysis states that the amount of a substance deposited or liberated at any electrode is directly proportional to the quantity of electricity passed through the electrolyte (solution) **(Wilcox and Gabe, 1992)**. The amount of substance can be calculated using the formula:

$$Q = I \times t \tag{1}$$

where Q is the total electric charge, I is the current, and t is the time. From the CV (**Figure 3f**) in the main manuscript, the current I is -1.95 nA and the time t is 1 s (since we need to calculate the production of the molecular oxygen per second), Q can be calculated as follows:

$$Q = -1.95 \times 10^{-9}\ C$$

Then by utilizing the Faraday's law, the amount of substances (n) in moles can be calculated as follows:

$$n = \frac{Q}{F \times v} \tag{2}$$

where v is the valency of the ions (for the reduction of oxygen, v = 4), and F is Faraday's constant (96485 C/mol). Thus n can be calculated as:

$$n = \frac{-1.95 \times 10^{-9}\ C}{4 \times 96485\ C/mol} = -5.05 \times 10^{-15}\ mol$$

Since the current value is negative, it means that the reaction is reduction (gain of electrons). However, the amount of substance cannot be negative, so the value should be absolute. Therefore, the amount of molecular oxygen produced is approximately 5.1 femtomoles. To convert the amount of molecular oxygen from moles to molecules, Avogadro's number (N_A) can be used which is approximately 6.022×10^{23}. The conversion can be done as follows:

$$n_{molecules} = n_{moles} \times N_A \tag{3}$$

By applying this formula, we obtain:

$$n = 5.05 \times 10^{-15} \times 6.022 \times 10^{23} = 3042675027$$

So, the rate of production of molecular oxygen is approximately 3.04×10^9 molecules/s. This value represents the total O_2 generation rate for the entire 21-electrode protonator array, as the measured current already reflects the combined contribution of all electrodes.

1.7. Working principle of the lactate & pH sensors

Enzymes have long served as the foundation for lactate biosensors due to their highly specific and efficient catalytic interaction with lactate. Among the various enzyme families involved in lactate metabolism, LOx is most widely used because of its strong substrate specificity and rapid turnover rate **(Madden et al., 2022).** The operational principle of LOx-based sensors relies on the enzymatic oxidation of lactate to pyruvate, accompanied by the generation of H_2O_2 as a by-product **(Fig. 1d)**, according to the following reaction:

$$Lactate + O_2 \xrightarrow{LOx} Pyruvate + H_2O_2 \quad (4)$$

When an appropriate potential is applied, the produced H_2O_2 undergoes oxidation or reduction at the electrode surface, yielding a current directly proportional to its concentration. This current response provides an indirect electrochemical measure of lactate levels in biological samples such as saliva.

$$H_2O_2 \rightarrow O_2 + 2H^+ + 2e^- \quad \text{(Oxidation)} \quad (5)$$
$$H_2O_2 + 2H^+ + 2e^- \rightarrow 2H_2O \quad \text{(Reduction)} \quad (6)$$

The electrochemical pH sensor, on the other hand, operates based on the reduction of gold oxide formed on the electrode surface during potential cycling. Changes in solution pH influence the reduction potential of gold oxide, thereby altering the measured electrode potential. This shift follows the Nernstian relationship, which describes the dependence of electrode potential on ionic activity **(Vidal-Iglesias et al., 2012).** As the proton concentration in solution varies, the potential across the electrode interface adjusts accordingly, allowing the pH to be determined electrochemically **(Daly et al., 2021).** For a pH sensor utilizing the gold oxide reduction mechanism, the Nernst equation can be expressed as **(Steinhauser et al., 2018):**

$$E = E^0 - 2.303 \times \frac{RT}{nF} \times pH \quad (7)$$

where E is the electrode potential under given conditions, E^0 is the standard electrode potential, R is the universal gas constant, T is the absolute temperature, n is the number of electrons involved in the reduction process, and F is Faraday's constant. This relationship allows the quantitative correlation between the measured electrode potential and the pH of the solution.

1.8. SEM, EDX and AFM analysis of the electrochemical sensor

Comprehensive surface characterization of the electrodes was carried out using SEM, EDX, and AFM to evaluate their morphological features, elemental composition, and topographical changes after each modification step. **Fig. S2** presents representative SEM micrographs, EDX spectra, and 3D AFM images (including cropped top-surface views) corresponding to the bare Au electrode and its subsequent modification stages. The bare gold electrode **(Fig. S2a$_1$)** exhibited a relatively smooth surface with mild undulations and shallow pits. Following Pt-black (Pt-B) deposition **(Fig. S2b$_1$)**, the electrode surface became densely covered with nanoscale platinum clusters, significantly enhancing the effective surface area by approximately 350 nm relative to bare Au. The Pt-B/o-PD/β-CD and Pt-B/o-PD/β-CD/LOx electrodes **(Fig. S2c$_1$ and S2d$_1$)** displayed similar granular morphologies, with no major visual distinctions observable under SEM, necessitating further confirmation through EDX analysis. The EDX spectrum of the unmodified electrode **(Fig. S2a$_2$)** primarily shows gold (Au) and silicon (Si) peaks. In contrast, the Pt-B modified surface **(Fig. S2b$_2$)** displays a strong Pt signal, verifying the successful electrodeposition of platinum. Upon further modification with o-PD/β-CD and LOx, additional carbon (C) and oxygen (O) peaks appear **(Fig. S2c$_2$ and S2d$_2$)**, corresponding to the organic polymer and enzyme layers. The elevated C and O intensities in **Fig. S2d$_2$** confirm the immobilization of LOx on the electrode surface, as further supported by **Fig. S3**.

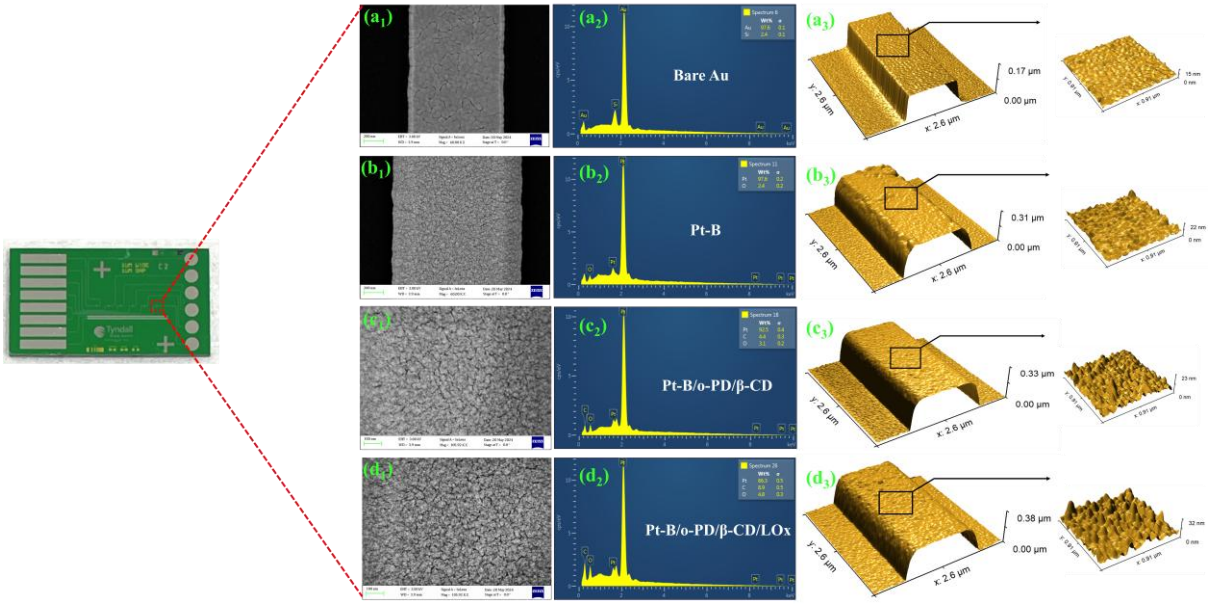


Fig. S2. SEM, EDX elemental spectra and three-dimensional AFM image of the electrodes surfaces are shown. (a_1, a_2, a_3) The bare Au electrode. (b_1, b_2, b_3) Pt-B. (c_1, c_2, c_3) Pt-B/o-PD/β-CD. (d_1, d_2, d_3) Pt-B/o-PD/β-CD/LOx modified electrodes.

EDX mapping was performed on randomly selected regions for each stage of electrode surface modification namely bare Au, Pt-B, Pt-B/o-PD/β-CD, and Pt-B/o-PD/β-CD/LOx. The elemental distributions of Au, Si, Pt, O, and C within these mapped areas showed uniform dispersion across the surfaces, with no evidence of significant clustering or aggregation, as illustrated in **Fig. S3a-e**. Complementary quantitative elemental data obtained from point-based EDX analysis for each modification step are summarized in **Table S1**, confirming the expected compositional changes accompanying each electrode treatment.

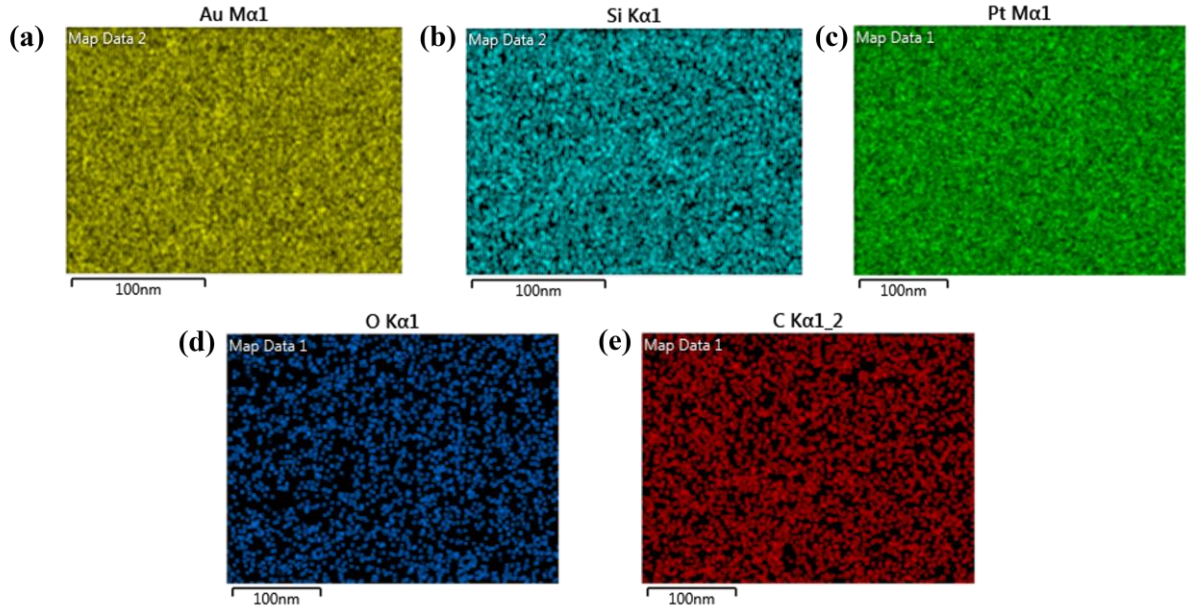


Fig. S3. An EDX element mapping images of (a) Gold. (b) Silicon. (c) Platinum. (d) Oxygen. (e) Carbon.

Table S1. Elemental analysis obtained with EDX at the bare Au, modified Pt-B, Pt-B/o-PD/β-CD, and Pt-B/o-PD/β-CD/LOx.

Layer	Element	Weight %	Atomic %
Au	Au	97.6	85.2
	Si	2.4	14.8
Pt-B	Pt	97.6	76.9
	O	2.4	23.1
Pt-B/o-PD/β-CD	Pt	92.5	45.8
	C	4.4	35.4
	O	3.1	18.8
Pt-B/o-PD/β-CD/LOx	Pt	86.3	29.8
	C	8.9	50.0
	O	4.8	20.2

AFM analysis provided complementary topographical information **(Fig. S2a$_3$-d$_3$)**. The bare Au electrode exhibited a uniform surface with an average thickness of 0.17 µm and RMS roughness of 70.07 nm **(Table S2)**. Upon Pt-B modification, the surface height increased to 0.31 µm, with roughness rising to 134.0 nm. The LOx-modified electrode (Pt-B/o-PD/β-CD/LOx) displayed the highest thickness (0.38 µm) and RMS roughness of 154.9 nm, reflecting the added enzyme and polymer layers. Collectively, the SEM, EDX, and AFM findings demonstrate consistent morphological and compositional evolution throughout the modification process, confirming the successful stepwise functionalization of the Interdigitated microelectrode (IDE) surface and validating the electrode's suitability for biosensing applications.

Table S2. RMS roughness obtained from AFM for different surfaces of the electrode.

Surface	**RMS Roughness (Sq) nm**
Bare Au	70.07
Pt-B	134.0
Pt-B/o-PD/β-CD	139.0
Pt-B/o-PD/β-CD/LOx	154.9

1.9. Electrochemical characterizations

The operational performance of the IDEs was verified by CV in 1 mM FCA across six electrodes on the same chip **(Fig. S4a)**. The resulting CVs exhibited a diffusion-limited current response, characteristic of large microelectrode behavior. This arose from the overlapping of radial diffusion zones between adjacent microbands, which merge to form a planar diffusion layer around the array**.** The IDEs demonstrated excellent inter- and intra-chip reproducibility, with a relative standard deviation (RSD) of 0.3% for the limiting current measured at 0.2 V vs. Pt. The generation of an average current of approximately 8.5 nA confirmed effective electron transfer and validated the functionality of the on-chip RE and CE electrodes. A typical optical micrograph of a single sensor after the full fabrication process is presented in the inset of **Fig. S4a.** The image shows that the sensing IDEs consisted of 20 microbands, while the protonator IDEs contain 21 microbands. The well-defined electrode edges and the absence of visible short circuits between the two arrays confirmed the high fidelity and reproducibility of the photolithography and lift-off steps. Each gold microband was 1 μm wide with a 1 μm interspacing, and the sensing array was positioned 2 mm from the gold CE to minimize interference from electrolysis products and local pH variations near the CE during electrochemical testing. Electrical connections between the electrodes and the potentiostat were made through gold peripheral leads integrated on the chip. Further characterization was carried out using the generator-collector (GC) mode as presented in **Fig. S4b**. In this configuration, the generator IDEs oxidized FCA to produce FCA^+ ions, which diffused across the 1 μm gap to the collector IDEs, where they were reduced back to FCA and this cycling could happen multiple times. The GC voltammograms displayed quasi steady-state profiles, consistent with the electrochemical behavior of ultramicroelectrode arrays. The collection efficiency, calculated as the ratio of collector to generator currents, was approximately 82%, suggesting that for pH control ~82% of protons generated at the protonator IDEs would reach the sensing IDEs, confirming the system's capacity for efficient local pH control. Optimization studies were subsequently performed to determine the ideal o-PD and LOx concentrations for sensor modification. Three o-PD concentrations (5, 10, and 15 mM) were tested **(Fig. S4c)**. The 10 mM concentration yielded the highest current response, likely due to optimal surface coverage that promotes efficient H_2O_2 oxidation/reduction. At lower o-PD concentrations, insufficient monomer availability limited polymer film formation, whereas excessive concentrations can oversaturate the electrode surface, hindering analyte diffusion. Similarly, varying LOx concentrations (5, 10, and 15 mg/mL) were evaluated and the optimal enzyme concentration was identified as 10 mg/mL, providing the maximum amperometric signal as depicted in **Fig. S4d**. Higher enzyme loadings led to diminished responses, likely due to enzyme overcrowding on the surface, which restricted catalytic activity and electron transfer. The influence of pH on enzyme performance was also examined between pH 5.0 and 8.5 in the presence of 2 mM lactate which is shown in **Fig. S4e.** The optimal LOx activity was observed at approximately pH 7.5. Following each stage of the fabrication process, specific techniques were utilized to meticulously analyze the modifications in surface properties.

Since H_2O_2 is generated enzymatically during the interaction of lactate by LOx, preliminary CV studies were performed in 0.8 mM H_2O_2 to assess the electrochemical behavior of the electrode surfaces **(Fig. S4f)**. The Pt-B modified electrode exhibited a marked increase in oxidation current, approximately 40 nA higher at 0.2 V vs. Pt compared to the bare gold electrode, reflecting the significantly larger electroactive surface area imparted by the Pt-B nanostructuring. Upon deposition of the o-PD/β-CD composite layer (green curve), redox currents declined noticeably. This reduction in current is consistent with the formation of a semi-permeable o-PD film, which partially restricts electron transfer while still permitting the diffusion of H_2O_2 molecules to the underlying Pt surface **(Wang et al., 2017).** Subsequent CV

measurements conducted in 1 mM FCA further confirmed this behavior, as illustrated in **Fig. S4g**, where an additional decrease in redox current was observed following LOx immobilization, as expected due to the added enzyme layer that increases charge transfer resistance. EIS data presented in **Fig. S4h** complement these findings, revealing consistent trends in charge transfer properties across each modification stage. A pronounced reduction in charge transfer resistance (Rct) was observed after Pt-B deposition, decreasing from approximately 26.5 MΩ at the bare Au surface to 0.05 MΩ (**Fig. S4h: inset**), demonstrating improved electron conductivity and reduced diffusion resistance resulting from the enlarged Pt surface area. The equivalent circuit model used to fit the impedance spectra is displayed in the inset of **Fig. S4h**. Following the deposition of the o-PD/β-CD/LOx film, a complete semicircular response could not be fitted, indicating a substantial increase in overall impedance, consistent with the presence of the enzyme-polymer matrix that acts as a kinetic barrier to charge transfer **(Madden et al., 2021)**.

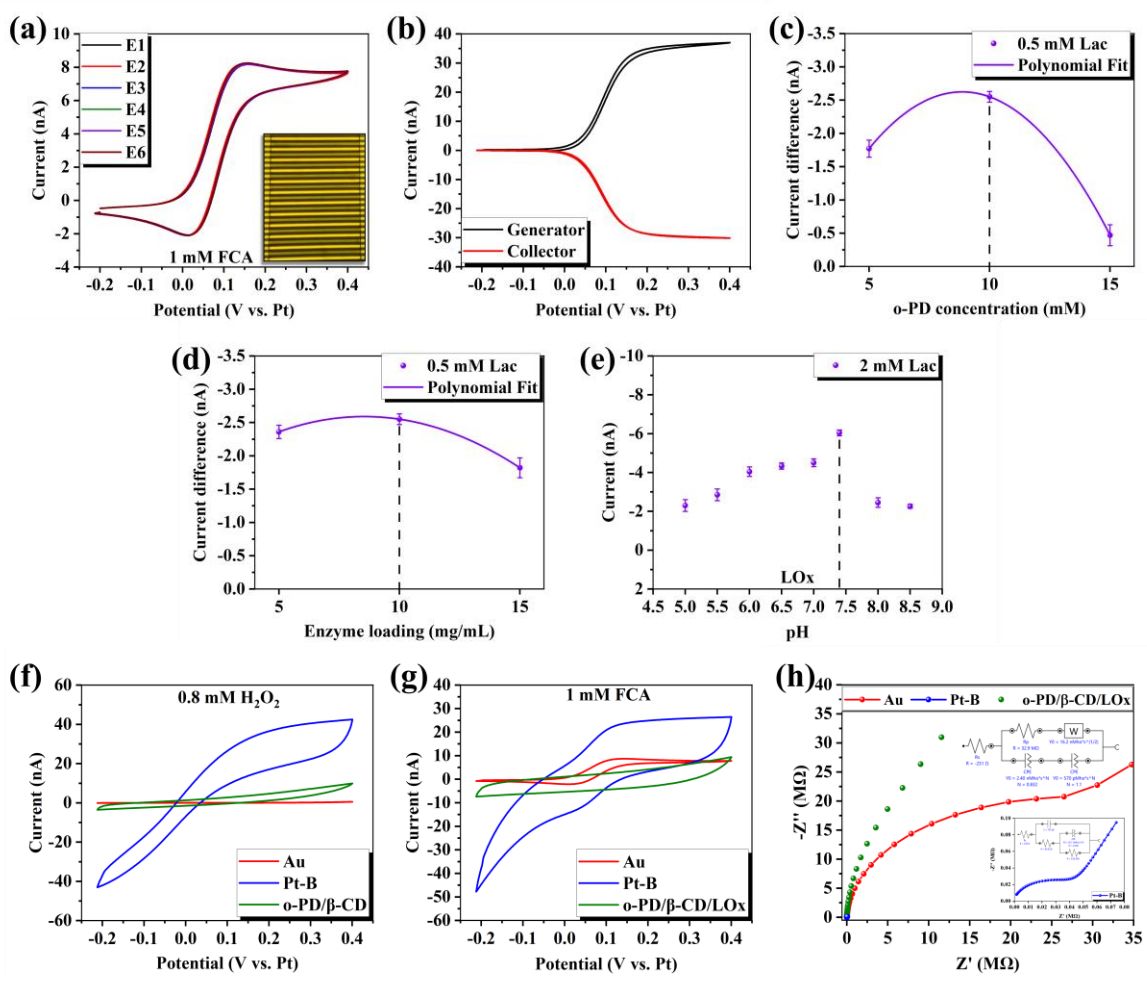


Fig. S4. (a) Three averaged cyclic voltammogram (CV) of 1 mM ferrocenecarboxylic acid (FCA) in 10 mM phosphate buffer (PB) measured for six different working electrodes on a single chip at a scan rate of 50 mV/s using on-chip Pt reference electrode, with the inset showing a 20x optical image of a single sensor comprising an interdigitated microband array. (b) CVs at gold IDEs of 1 mM FCA in 10 mM PB at a scan rate of 50 mV/s in one working electrode in generator-collector format. The generator IDEs (black) was cycled between -0.2 V and 0.4 V while the collector IDEs (red) was held at a potential of 0 V. (c) Current

responses for 0.5 mM lactate measured at a Au/Pt-B/o-PD/β-CD/LOx modified electrode surface (while maintaining the concentrations of LOx and β-CD were kept constant at 10 mg/mL and 15 mM, respectively), where the o-PD concentration was varied (5 mM, 10 mM, and 15 mM), in 50 mM PB (pH 7.4). Purple line is a guide to the eye. (d) Optimisation of LOx enzyme loading in 0.5 mM lactate concentration. Purple line is a guide to the eye. (e) Effect of pH on lactate oxidase activity. (f) CVs in 0.8 mM H_2O_2 at a scan rate of 50 mV/s were recorded at the bare gold (red), Pt-B modified (blue), and o-PD/β-CD modified (green) microband array electrodes versus on chip Pt reference. (g) CVs in 1 mM FCA at a scan rate of 50 mV/s were recorded at the bare gold (red), Pt-B modified (blue), and o-PD/β-CD/LOx modified (green) microband array electrodes versus on chip Pt reference. (h) Nyquist plots from the corresponding EIS measurements in 1 mM FCA were obtained at the bare gold (red) [Rct 26.5 MΩ], Pt-B modified (blue) [Rct 0.05 MΩ], and o-PD/β-CD/LOx modified (green) [unfitted data] electrodes versus on chip Pt reference. The inset shows the equivalent circuit used for the bare gold and Pt-B modified electrodes, respectively.

1.10. Simulation of local pH modulation

Numerical simulations were performed to evaluate the generation and diffusion of protons from the protonator IDEs used for local pH control in the lactate sensing system. The model was constructed in COMSOL Multiphysics 5.5 using finite element analysis (FEA) to capture proton transport under galvanostatic conditions. The simulated geometry represented a 3 mm microenvironment containing two interdigitated electrode arrays, one functioning as the protonator and the other as the sensing interface. Each array consisted of 1 μm wide, 150 nm high microbands separated by 1 μm gaps. A steady anodic current was applied at the protonator electrodes to generate protons electrochemically, which then diffused across the narrow interelectrode gap to the sensing region. The flux of protons released was defined as proportional to the applied current, in accordance with Faraday's law:

$$Flux = \frac{i}{F \times A} \tag{8}$$

where i is the applied current, F is the Faraday's constant, and A is the surface area of the electrodes. The initial bulk pH was set to 7.0, and the diffusion of protons through the electrolyte was modeled using a diffusion coefficient of 9.31×10^{-5} cm^2 s^{-1} **(Lee and Rasaiah, 2011).** Proton transport and the resulting pH gradient were governed by Fick's second law and solved under steady-state conditions **(O'Sullivan et al., 2021).** This simulation provided insight into the spatial and temporal evolution of pH within the sensing zone, enabling optimization of the local environment for enzyme activity and lactate detection. It is important to note that the objective of this simulation is not to overcome the oxygen limitation inherent to oxidase-based sensing. Dissolved oxygen availability determines the maximum enzymatic turnover rate of lactate oxidase under static conditions. In contrast, the purpose of local electrochemical pH modulation is to control the enzyme microenvironment at the electrode-solution interface, where enzymatic activity and electrochemical signal generation occur. Local pH variations influence enzyme activity, interfacial charge transfer, and signal stability within the diffusion layer, even when bulk oxygen concentration remains unchanged. In addition, a pH sensor was developed and characterized separately over a pH range of 3 to 9 in buffer-based media to validate and support the simulation outcomes.

To evaluate the effectiveness of the proposed in-situ electrochemical pH control using IDEs, finite element method (FEM) simulations were performed in COMSOL Multiphysics. The simulations were performed using an aqueous saliva-mimicking electrolyte (initial pH ≈ 7.0) containing a weak monoprotic buffer (0.1 mM, pKa = 6.1). Acid-base equilibria, water autoprotolysis, and diffusion of H^+/OH^- species were included. Electrochemical pH modulation was implemented as a proton flux boundary condition at the electrode surface, corresponding to the applied current density. The model was designed to simulate proton generation and diffusion from a protonator IDE and to determine the optimal electrode configuration and operating parameters required for achieving precise local pH control. In this simulation, a galvanostatic current bias was applied to the protonator array to induce proton flux. **Fig. S5a** shows a 2D cross-sectional representation of a 260 × 300 µm region intersecting the interdigitated array, illustrating the local pH profile after a 500 nA current was applied for 0.01 s. While the bulk solution retains its initial pH of 7.0, the local pH in the vicinity of the electrodes decreases to approximately 6.6, as reflected by the color variation in the simulation. The enlarged 5 × 5 µm inset clearly depicts this localized acidification adjacent to the electrode edges. When the current bias was maintained for 0.5 s, the diffusion zone expanded, and the pH near the IDEs decreased further to ~6.3, as shown in **Fig. S5b**. After 2 s of bias application **(Fig. S5c)**, the proton diffusion layer thickened substantially, reducing the local pH to around 6 in the vicinity of the electrode surface. These results demonstrate that the local pH environment can be rapidly and precisely tuned by adjusting the applied current and duration, achieving effective pH control within 2 seconds. The method enables real-time pH adjustment to the optimal level for LOx activity, thereby minimizing potential inaccuracies due to variations in the bulk solution pH. Furthermore, the concurrent generation of molecular oxygen during protonation offers an additional benefit by potentially enhancing the enzymatic reaction (by regenerating reduced enzyme) and overall sensor performance. We note that this approach eliminates the need to add a mediator molecule, such as a ferrocene derivative.

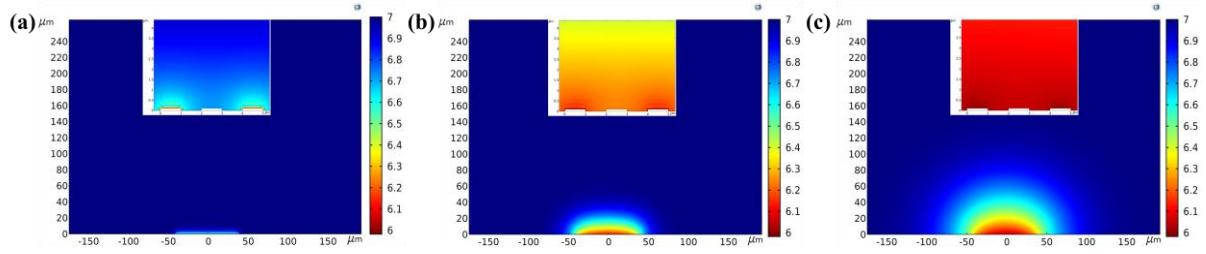


Fig. S5. COMSOL simulation of a gold interdigitated microband array electrodes with a current of 500 nA applied to the protonator electrode. The simulated pH profile after (a) 0.01 s. (b) 0.5 s. (c) 2 s of current imposition. The insets show the higher magnification of the three electrodes representing the local pH environment. The colour legends on the right indicate the pH. The axis for each simulation is given in micrometers.

1.11. Effects of interference species in buffer solution

Table S3 summarizes the interference study conducted with and without β-cyclodextrin (0 and 15 mM). The data clearly indicate that incorporating 15 mM β-CD markedly suppresses interference from 0.5 mM AA, UA, D-fruc, D-glu, and Ace in both 2 mM and 5 mM lactate solutions. In contrast, the absence of β-CD results in the highest levels of signal disturbance. This behavior is further illustrated in **Fig. S6**, which compares the chronoamperometric responses recorded for 5 mM lactate in the presence of the five interferents. **Fig. S6a** (no β-CD) shows that introducing interferents at 200 s produces a noticeable current deviation of approximately 10–15%, highlighting the vulnerability of the LOx-based sensor without the protective β-CD layer. Once β-CD is incorporated **(Fig. S6b)**, however, the influence of the same interferents is reduced dramatically, with signal changes limited to only 2-3%. Overall, these results confirm that the Au/Pt-B/o-PD/β-CD/LOx configuration provides strong anti-interference capability, enabling reliable lactate sensing even in the presence of electroactive species commonly found in saliva and other biological fluids.

Table S3. Table of interfering species.

Interfering Species	β-cyclodextrin Concentration (mM)	Lactate Concentration (mM)	Interferent Concentration (mM)	(Io/I×100)* (%)
L-Ascorbic Acid	0	5	0.5	94.83
Uric Acid				85.26
D-(+)-Fructose				94.62
D-Glucose				96.15
Acetaminophen				108.14
L-Ascorbic Acid	**15**	**5**	**0.5**	**97.11**
Uric Acid				**97.65**
D-(+)-Fructose				**97.46**
D-Glucose				**96.39**
Acetaminophen				**102.40**
L-Ascorbic Acid	**15**	**2**	**0.5**	**98.28**
Uric Acid				**97.31**
D-(+)-Fructose				**97.15**
D-Glucose				**96.25**
Acetaminophen				**103.49**

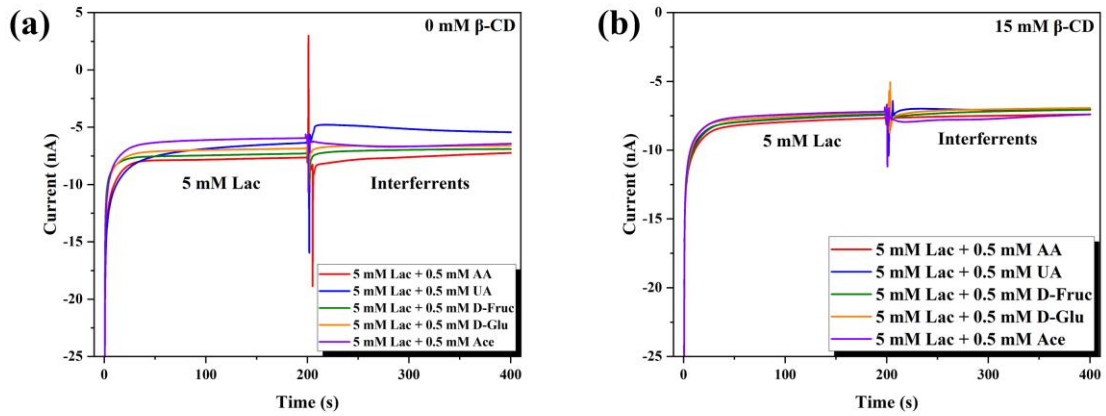


Fig. S6. Chronoamperometric (CA) responses obtained from (a) 0 mM β-CD. (b) 15 mM β-CD surfaces in 5 mM lactate (10 mM PB, pH 7.4) and aliquots of 5 mM lactate with other potential interfering species (L-ascorbic acid (AA), uric acid (UA), D-fructose (D-Fruc), D-glucose (D-Glu), and Acetaminophen (Ace)) added after 200 s of the measurement.

1.12. Lactate and pH monitoring in artificial and calf saliva

Fig. S7a shows the CA responses of the Au/Pt-B/o-PD/β-CD/LOx modified electrodes recorded at -0.25 V for 60 s across different lactate concentrations. The current increased proportionally with lactate concentration, confirming a clear concentration-dependent response. To evaluate whether in-situ pH regulation improved sensor performance, the protonator IDEs were biased at 1.05 V, and identical lactate measurements were performed under pH-controlled conditions **(Fig. S7b)**. The resulting curves show that the current response was consistently enhanced at pH 6.0 through the production of molecular oxygen, demonstrating that pH control improved the electrochemical detection of lactate in saliva.

Gold oxide reduction peaks were recorded over the potential window of -0.4 to 0.8 V, with three replicate scans obtained at each pH value to ensure reproducibility **(Fig. S7c)**. The expanded view of the reduction region depicts in **Fig. S7d** shows the expected anodic shift in the peak potential as the pH decreases. However, the voltammograms recorded in saliva exhibited noticeable distortions such as altered peak intensities, shifts in peak position, and changes in shape, consistent with the effects of increased viscosity on electron-transfer kinetics and diffusion-controlled processes **(Adib et al., 2025).**

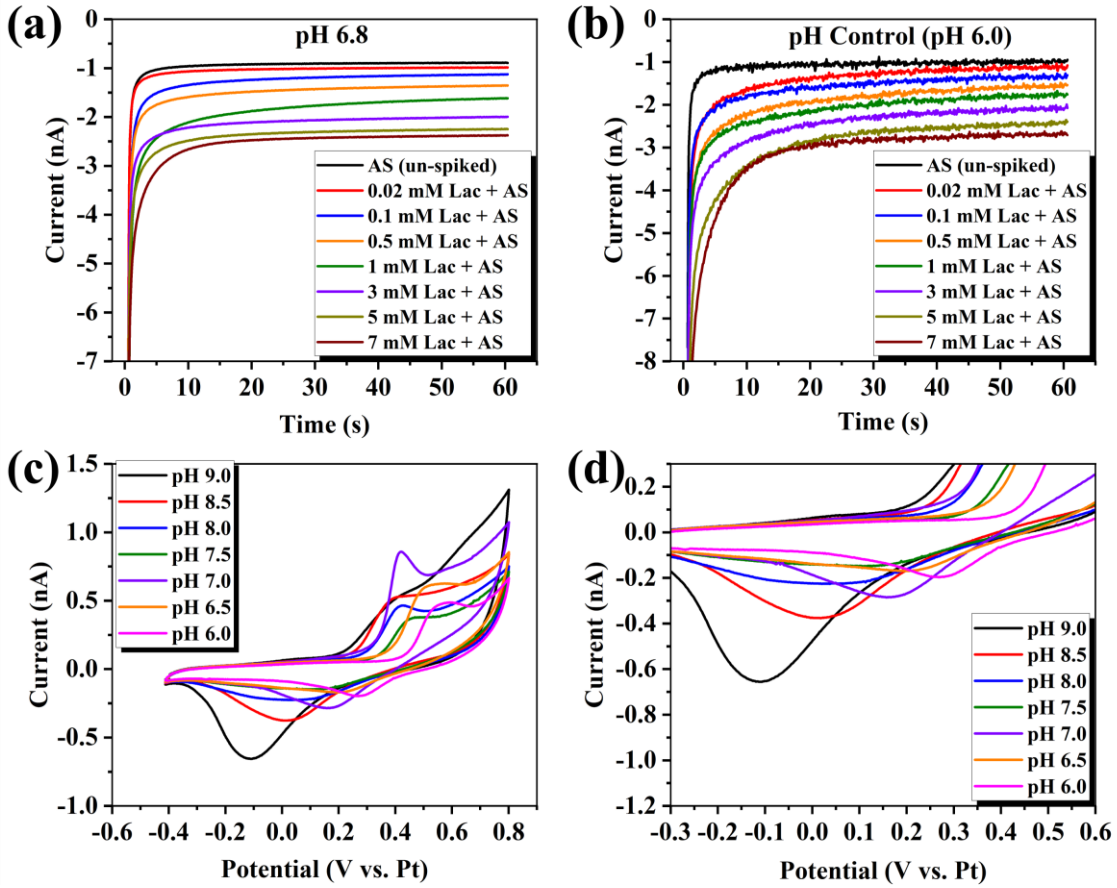


Fig. S7. CA responses obtained from the lactate biosensor in artificial saliva with the known concentrations of lactate. (a) At pH 6.8. (b) At pH 6.0 by controlling the pH from pH 6.8 through biasing the protonator array electrodes at 1.05 V. (c) CVs of gold oxide reduction peaks obtained at a gold interdigitated microband electrodes in artificial saliva pH solution ranging from pH 6 to 9 with platinum reference electrode at a scan rate of 100 mV/s. (d) Expanded view highlighting the reduction peaks for pH 6 - 9.

1.13. Lactate monitoring in calf saliva and statistical analysis

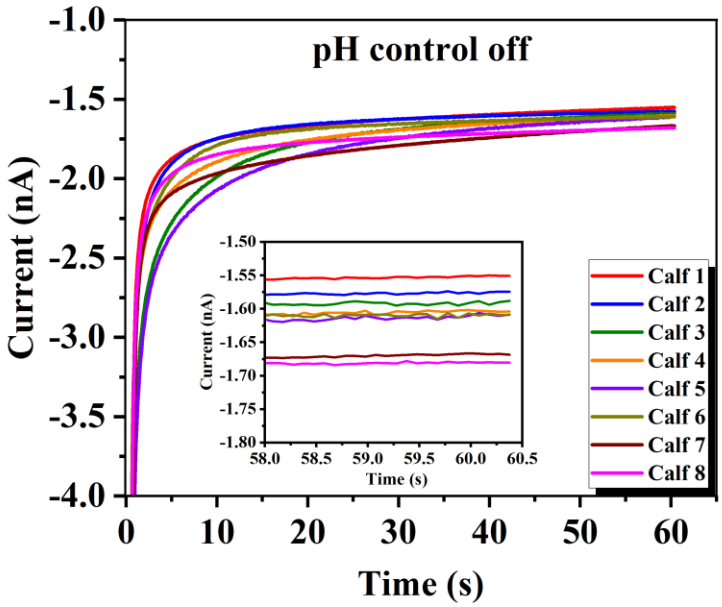


Fig. S8. CAs from the lactate sensor in real saliva samples from eight calves to determine the lactate level in saliva while pH control is off. Inset shows the last 2 seconds of CA measurements for all the calves samples.

A least-squares linear regression analysis was conducted between the proposed sensor (Y) and the commercial analyzer (X), where the slope was calculated as:

$$m = \frac{\sum(X-\bar{X})(Y-\bar{Y})}{\sum(X-\bar{X})^2} \quad (9)$$

and the intercept (b) was determined from:

$$b = \bar{Y} - m\bar{X} \quad (10)$$

The coefficient of determination (R^2) was calculated using the Pearson correlation coefficient:

$$R^2 = r^2 \quad (11)$$

Linear regression yielded:

$$Y = 0.937X + 48.23 \text{ with } R^2 = 0.987$$

In addition, the mean absolute error (MAE) was calculated as:

$$MAE = \frac{1}{n}\sum|Y - X| \quad (12)$$

Resulting in MAE = 16.5 µM, corresponding to an average relative error of 2.32%. These results demonstrate excellent agreement between the proposed biosensor and the commercial Lactate Pro 2 analyzer, with high correlation (R^2 = 0.987), minimal systematic deviation (slope

≈ 0.94), and low average relative error (2.32%). This confirms the analytical accuracy and reliability of the developed platform for real saliva measurements.

Table S4. Lactate concentrations in real saliva samples measured with the Au/Pt-B/ o-PD/β-CD/LOx biosensor and validate with a commercial lactate meter (Lactate Pro 2).

Samples	Calf ID	Current (nA)	Lactate Concentration (µM)	Commercial Lactate Meter Measurement (µM)	Calf Health Visualization
Calf-1	1887	-1.571	586 ± 10	600 ± 70	Healthy
Calf-2	1889	-1.582	619 ± 8	600 ± 60	Healthy
Calf-3	1893	-1.592	650 ± 9	620 ± 50	Healthy
Calf-4	1910	-1.604	689 ± 10	700 ± 40	Healthy
Calf-5	1900	-1.611	713 ± 9	700 ± 80	Healthy
Calf-6	2049	-1.609	706 ± 10	700 ± 100	Healthy
Calf-7	**2218**	**-1.673**	**966 ± 8**	**1000 ± 100**	**Sick**
Calf-8	**2202**	**-1.681**	**1005 ± 10**	**1000 ± 120**	**Sick**

Table S5. Lactate concentrations in real saliva samples measured with the Au/Pt-B/o-PD/β-CD/LOx biosensor using Autolab and benchmarked with a commercial lactate meter (Lactate Pro 2).

Samples	Calf ID	Current (nA) pH control off	Lactate Concentration (µM) pH control off	Current (nA) pH control on	Lactate Concentration (µM) pH control on	Commercial Lactate Meter Measurement (µM)	Calf Health Visualization
Calf-6	2049	-1.609	706 ± 10	-1.842	703 ± 12	700 ± 100	Healthy
Calf-8	2202	-1.681	1005 ± 10	-1.928	1036 ± 15	1000 ± 120	Sick

1.14. Calves body health scores

Table S6 shows the calves body health scores.

Table S6. Calves body health scores.

Samples	Calf ID	Demeanour	Eyes	Ears	Nose	Cough	Dehydration	Mobility	Interest in Surroundings	Faecal (cleanliness)	Naval
Calf-6	2049	0	0	0	0	0	0	0	0	0	1
Calf-8	2202	2	1	1	1	0	2	1	2	1	1

1.15. Comparison of sensor data with other lactate sensor literatures

Table S7 shows the comparison of different enzymatic lactate sensors performances with the proposed lactate sensor in artificial saliva.

Table S7. Comparison of the analytical performance of different enzymatic lactate sensors in saliva reported in the literature.

Electrode materials	Biofunctionalization	Sensing type	Linearity range (mM)	Sensitivity (S)	Limit of detection (µM)	Reference
LSG/Pt	CS/LOx	Amperometric	0.2 – 3	39.3 $\mu A.mM^{-1}.cm^{-2}$	110 (saliva)	(Madden et al., 2022)
Carbon paste	Fc/BSA/LOx	Amperometric	0.5 – 2	21.8 $\mu A.mM^{-1}.cm^{-2}$	-	(Liu et al., 2022)
SPE	PB/LOx	Chronoamperometric	0.025 – 0.25	-	10 (saliva)	(Petropoulos et al., 2016)
ZnO/GO	LOx	Chronoamperometric	0.2 – 2	3.30 $\mu A.mM^{-1}$	9 (saliva)	(Han and Shaohui, 2024)
AgNPs	BSA/GA/LOx	Amperometric	0.06–1.25	0.256 $\mu A.mM^{-1}.cm^{-2}$ (PBS)	-	(Abrar et al., 2016)
GCE	Pt/MXene/LOx	Amperometric	0.02 – 0.75	14.076 $\mu A.mM^{-1}$	10 (saliva)	(Xu et al., 2024)
PET	PB/o-PD/LOx	Amperometric	0.1−1.0	0.53 $\mu A.mM^{-1}$	50 (saliva)	(Kim et al., 2014)
Ti/Au/Pt	**o-PD/β-CD/LOx**	**Chronoamperometric**	**0.02-7 (AS)**	**-49.33 $\mu A.mM^{-1}.cm^{-2}$ (AS)**	**0.6 (AS)**	**This work**

Abbreviations: LSG: laser-scribed graphene, Pt: platinum, CS: chitosan, LOx: lactate oxidase, Fc: ferrocene, BSA: bovine serum albumin, SPE: screen-printed electrode, PB: prussian blue, ZnO: zinc oxide, GO: graphene oxide, AgNPs: silver nanoparticles, GA: glutaraldehyde, GCE: glassy carbon electrode, PET: poly(ethylene terephthalate), Ti: titanium, Au: gold, o-PD: o-phenylenediamine, β-CD: β-cyclodextrin, AS: artificial saliva.

1.16. Customized sensor electronics interface for electrochemical analysis

A custom-designed portable PCB potentiostat was developed to interface with the sensor system for tracking the Lactate and pH in calf saliva samples. This design was adapted from the Electrochemical Impedance Spectroscopy (EIS) Disease Detection System described in the thesis, with several hardware and firmware enhancements implemented to support a wider range of electrochemical techniques. The core of the system was the ADuCM355 System-on-Chip (SoC) from Analog Devices, an integrated solution that combines a high-performance ARM Cortex-M3 microcontroller with an analog front end (AFE) optimized for electrochemical sensing. The AFE incorporated precision digital-to-analog converters (DACs), transimpedance amplifiers (TIAs), analog-to-digital converters (ADCs), and multiplexers (MUX) for signal routing and conditioning. This configuration allowed precise excitation and readout of the working, reference, and counter electrodes, as illustrated in **Fig. S9a**. To accommodate multiplexed sensing, an on-PCB external analog multiplexer was connected to the ADuCM355, enabling the selection of specific working electrodes on the micro-SD-based sensor chip. This feature facilitates simultaneous or sequential measurements across multiple electrodes, thereby supporting multi-analyte detection within the same chip. The firmware developed for this platform enables several electrochemical measurement techniques, including cyclic voltammetry (CV), square wave voltammetry (SWV), differential pulse voltammetry (DPV), chronoamperometry (CA), and bipotentiostat chronoamperometry (BCA). These techniques could be selected and controlled digitally via a smart phone interface. For power management, the system operated from a 12 V DC input, regulated through a charger-battery-regulator chain that provided stable supply voltages of 5 V, 3.7 V, and 3.3 V DC, respectively **(Fig. S9b)**. The inclusion of a 3.7 V lithium-ion battery allowed portable operation, while the low-dropout regulator ensured a clean 3.3 V supply to the SoC and associated components. A Bluetooth Low Energy (BLE) 5.0 module (HC-42), based on the nRF52832 chipset from Nordic Semiconductor, enabled wireless communication between the potentiostat and an Android mobile device. The BLE interface communicated with the Cortex-M3 microcontroller via a universal asynchronous receiver-transmitter (UART) channel. Additional debugging and firmware updates were performed through the ADI J-Link OB emulator port, while status LEDs indicate the system's operating state. A dedicated Android application, developed using MIT App Inventor 2, allowed users to discover and connect to the BLE peripheral, select desired electrochemical techniques, set parameters, and receive real-time measurement data. The acquired data could be exported as .csv files for offline processing or shared directly through common platforms such as email, Google Drive, Telegram, or WhatsApp. This compact, low-power electronic interface thus serves as a fully portable potentiostat platform for real-time electrochemical sensing, combining the functionality of a laboratory-grade system with field-deployable convenience.

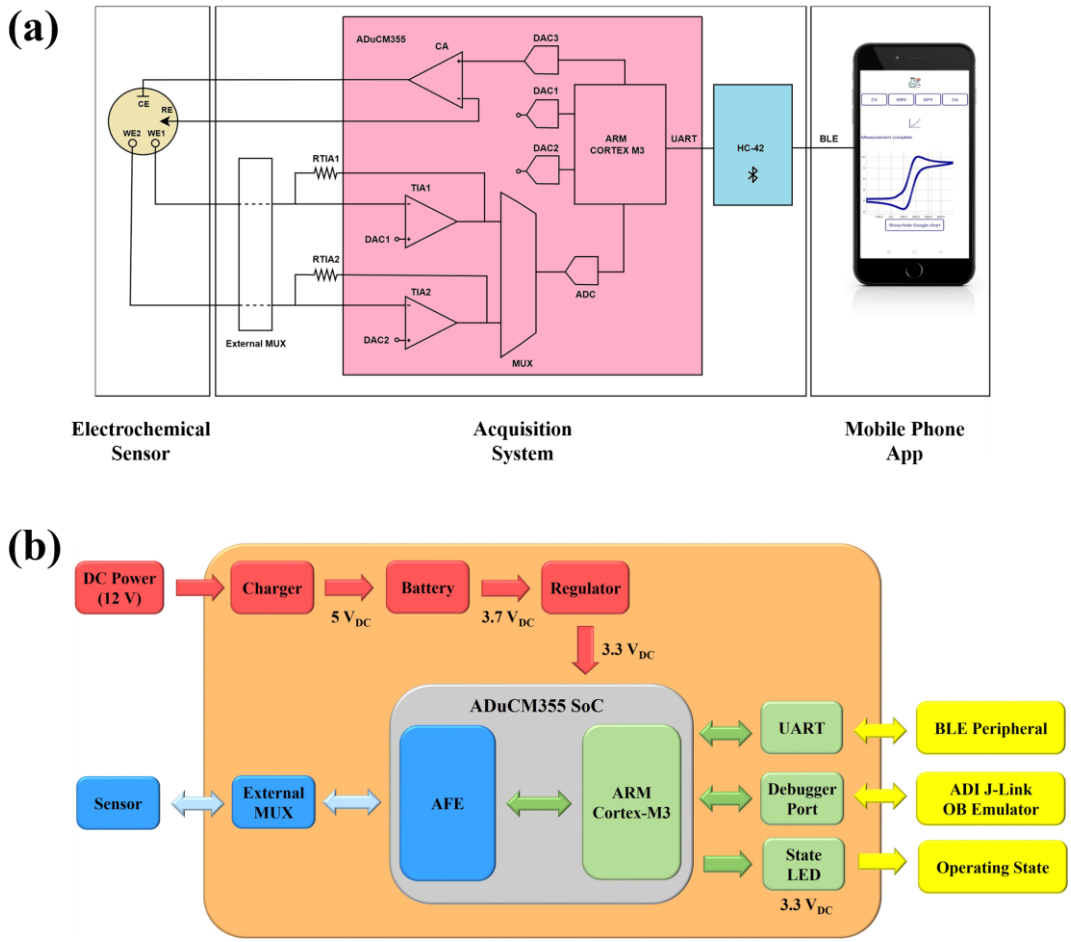


Fig. S9. (a) Simplified excitation and readout circuit interface. (b) Overall functional block diagram of the sensor interface electronics

1.17. Performance of portable sensor interface for salivary lactate and pH detection

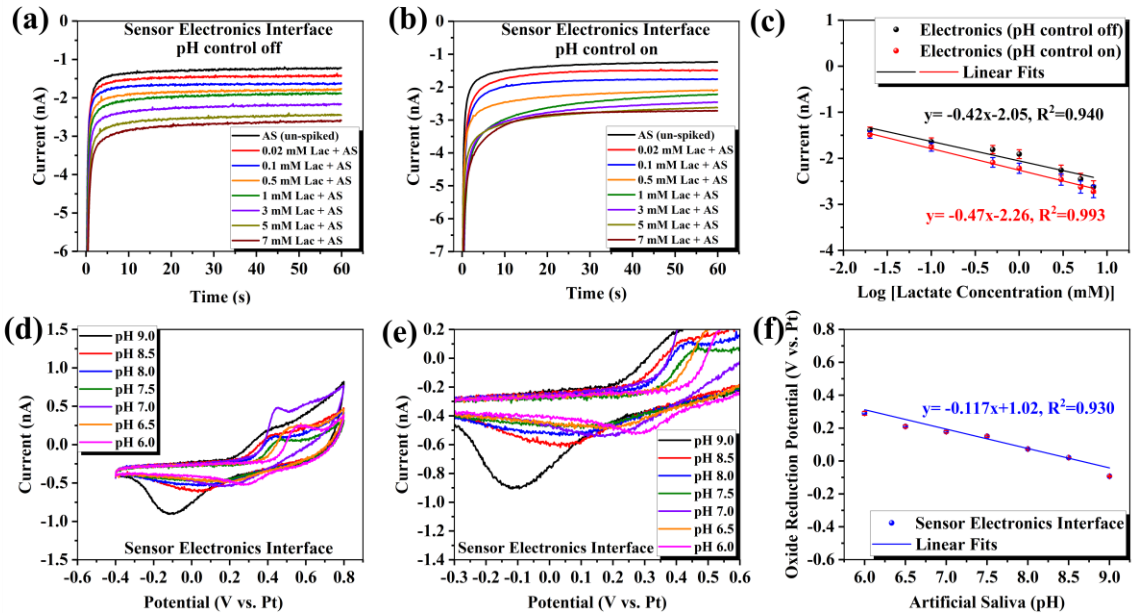


Fig. S10. Chronoamperometric responses obtained from the sensor electronics interface in artificial saliva with the known concentrations of lactate, while (a) pH control is off. (b) pH control is on. (c) Corresponding calibration plots and linear range in semi-log scale. (d) Cyclic voltammogram attained from bare gold electrodes in artificial saliva pH solutions ranging from pH 6.0 to 9.0 with on chip reference electrode at a scan rate of 100 mV/s by using sensor electronics interface. (e) Expanded view highlighting the reduction peaks for pH 6-9. (f) Resulting calibration plot.

1.18. Lactate detection in calf saliva using sensor electronics interface

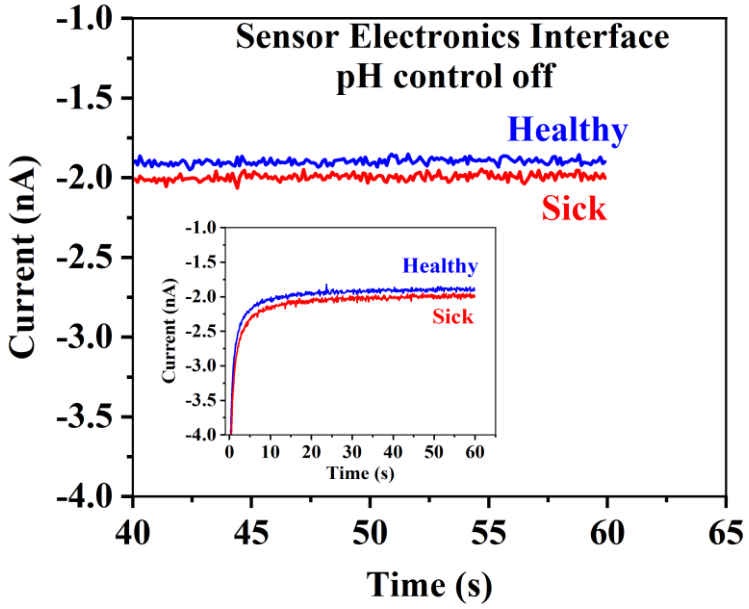


Fig. S11. CA responses during the last 20 s obtained from the lactate biosensor in calf saliva samples for lactate detection while pH control is off using sensor electronics interface. Inset shows the full CA traces for calf saliva samples.

1.19. Overall image of sensor electronics interface

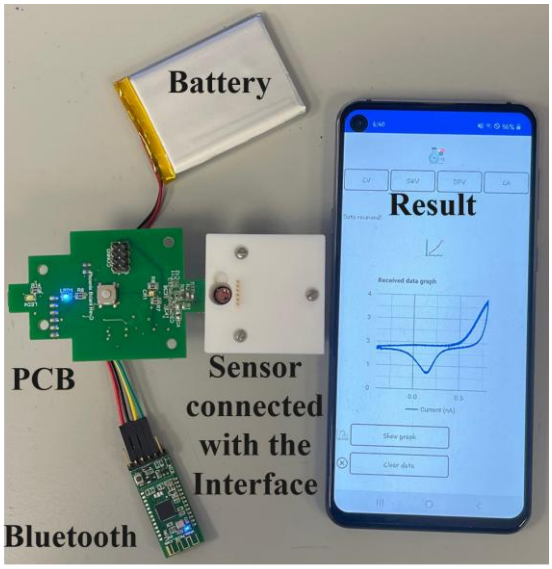


Fig. S12. A comprehensive view of the developed pH sensor along with its interface electronics.

1.20. Comparison tables

Table S8. Lactate concentrations in real saliva samples measured with the Au/Pt-B/o-PD/β-CD/LOx biosensor using Sensor Electronics Interface and benchmarked with a commercial lactate meter (Lactate Pro 2).

Samples	Calf ID	Current (nA) pH Control off	Lactate Concentration (µM) pH Control off	Current (nA) pH Control on	Lactate Concentration (µM) pH Control on	Commercial Lactate Meter Measurement (µM)	Calf Health Visualization
Calf-6	2049	-1.964	624 ± 50	-2.183	686 ± 36	700 ± 100	Healthy
Calf-8	2202	-2.060	1056 ± 35	-2.266	1029 ± 27	1000 ± 120	Sick

Table S9. Performance comparison of autolab and sensor electronics interface for pH sensing.

Samples	Calf ID	Autolab		Sensor Electronics Interface		Calf Health Visualization
		Voltage (V)	pH	Voltage (V)	pH	
Calf-6	2049	0.136	7.51	0.140	7.52	Healthy
Calf-8	2202	0.015	8.52	0.016	8.57	Sick

Reference

Abrar, M.A., Dong, Y., Lee, P.K., Kim, W.S., 2016. Sci Rep 6, 30565. https://doi.org/10.1038/srep30565

Adib, M.R., Barrett, C., O'Sullivan, S., Flynn, A., McFadden, M., Kennedy, E., O'Riordan, A., 2025. Biosensors and Bioelectronics 275, 117234. https://doi.org/10.1016/j.bios.2025.117234

Barrett, C., O'Sullivan, F., Barry, S., Grygoryev, K., O'Gorman, D., O'Mahony, C., O'Riordan, A., 2019. Presented at the 2019 IEEE SENSORS, IEEE, Montreal, QC, Canada, pp. 1–4. https://doi.org/10.1109/SENSORS43011.2019.8956509

Daly, R., Narayan, T., Shao, H., O'Riordan, A., Lovera, P., 2021. Sensors 21, 3544. https://doi.org/10.3390/s21103544

Han, J., Shaohui, J., 2024. Alexandria Engineering Journal 92, 171–175. https://doi.org/10.1016/j.aej.2024.02.040

Kim, J., Valdés-Ramírez, G., Bandodkar, A.J., Jia, W., Martinez, A.G., Ramírez, J., Mercier, P., Wang, J., 2014. Analyst 139, 1632–1636. https://doi.org/10.1039/C3AN02359A

Lee, S.H., Rasaiah, J.C., 2011. The Journal of Chemical Physics 135, 124505. https://doi.org/10.1063/1.3632990

Liu, M., Yang, M., Wang, M., Wang, H., Cheng, J., 2022. Biosensors 12, 210. https://doi.org/10.3390/bios12040210

Madden, J., Barrett, C., Laffir, F.R., Thompson, M., Galvin, P., O' Riordan, A., 2021. Biosensors 11, 249. https://doi.org/10.3390/bios11080249

Madden, J., Vaughan, E., Thompson, M., O' Riordan, A., Galvin, P., Iacopino, D., Rodrigues Teixeira, S., 2022. Talanta 246, 123492. https://doi.org/10.1016/j.talanta.2022.123492

O'Sullivan, B., Patella, B., Daly, R., Seymour, I., Robinson, C., Lovera, P., Rohan, J., Inguanta, R., O'Riordan, A., 2021. Electrochimica Acta 395, 139113. https://doi.org/10.1016/j.electacta.2021.139113

Petropoulos, K., Piermarini, S., Bernardini, S., Palleschi, G., Moscone, D., 2016. Sensors and Actuators B: Chemical 237, 8–15. https://doi.org/10.1016/j.snb.2016.06.068

Steinhauser, B., Vidal, C., Barb, R.-A., Heitz, J., Mardare, A.I., Hassel, A.W., Hrelescu, C., Klar, T.A., 2018. J. Phys. Chem. C 122, 4565–4571. https://doi.org/10.1021/acs.jpcc.7b11355

Vidal-Iglesias, F.J., Solla-Gullón, J., Rodes, A., Herrero, E., Aldaz, A., 2012. J. Chem. Educ. 89, 936–939. https://doi.org/10.1021/ed2007179

Wang, J., Wang, M., Guan, J., Wang, C., Wang, G., 2017. Materials Science and Engineering: C 71, 844–851. https://doi.org/10.1016/j.msec.2016.10.080

Wilcox, G.D., Gabe, D.R., 1992. Transactions of the IMF 70, 93–94. https://doi.org/10.1080/00202967.1992.11870951

Xu, M., Lu, C., Han, W., 2024. Alexandria Engineering Journal 100, 176–180. https://doi.org/10.1016/j.aej.2024.05.049